LA-UR-14-29077
Approved for public release; distribution is unlimited.

Title: Detecting Weak Explosions at Local Distances by Fusing Multiple Geophysical Phenomenologies

Author(s): Carmichael, Joshua Daniel
Nemzek, Robert James
Arrowsmith, Stephen John
Sentz, Kari

Intended for: Geophysical Journal International
Report

Issued: 2014-11-24

Detecting Weak Explosions at Local Distances by Fusing Multiple Geophysical Phenomenologies

Joshua D Carmichael, Stephen Arrowsmith, Robert Nemzek, Kari Sentz

November 20, 2014

Contents

List of Figures

0.1 Abstract

Explosion monitoring requires the technical capability to screen geophysical signatures of chemical explosions from those attributable to natural and non-threatening sources, like routine human activity or natural processes. This is particularly challenging at low signal strengths or large standoff distances, as standard detection methods that use single phenomenologies can produce marginal or absent detections. We addressed this challenge by recording coincident acoustic, seismic and radio frequency waveform signatures from high explosive experiments to determine how these signatures could be combined to increase explosion-screening capability. We thereby added real, observed noise to each signature's data stream and subsequently found that even highly sensitive correlation detectors missed detections when they were applied separately. By adding these temporally coincident statistics through Fisher's combined probability test, we increased our explosion-waveform screening capability. This resulting tests gave high-probability detections with zero false alarms. Further, including such fusion methods in routine monitoring operations will likely provide increased deterrence against evasive explosive testing.

1.1 Introduction

Explosions produce waveform signatures through several distinct geophysical phenomenologies as sources of electromagnetic, acoustic, and seismic radiation. The detection and identification of these signals can thereby provide evidence of explosive events that are otherwise unobservable. Such signatures are therefore used to discriminate natural geophysical sources (e.g., lightning) from those attributable to clandestine weapon testing or demolition activity, in operations supporting both nuclear detonation monitoring and active explosives mitigation. This discrimination procedure often requires processing noisy, digital geophysical data that is overwhelmingly comprised of natural and non-threatening signals. It is therefore important to develop statistically robust methods to reliably detect and screen explosion-triggered waveforms from such natural signals that can be evaluated through controlled experiments.

Previous work in explosion detection has largely focused on utilizing radio-frequency (RF) [21, 15], acoustic [36, 35] or seismic [22, 12] emission signatures separately. However, as explosion monitoring missions continually expand to target small, evasively conducted tests, fusing signals from separate phenomenologies will likely become crucial for source discrimination [3, 24]. This is particularly significant in scenarios whereby single phenomenological waveforms yield marginal or absent detections. For example, acoustic signals generated by above ground explosions may be undetectable at certain observation ranges because their propagation paths are determined by temporally variable atmospheric structure [4]. Associated seismic signals may also be difficult to identify if an explosion's air shock transmits only weakly into the ground, or preferentially excites high frequency energy ($\geq$ 25 Hz) that scatters and attenuates rapidly with propagation distance from the source (e.g., [25]). Further, RF emissions that are also produced by such explosions occupy a heavily cluttered signal environment that is largely dominated by broadcast and communications signals ($\sim$10 kHz-1 GHz) which interfere with these explosion-generated waveforms [15]. Cumulatively, these factors comprise practical challenges for detecting small explosions that become more serious at smaller yields and larger standoff distances [8]. Additional research is necessary to assess if individual detection statistics, computed from single phenomenologies, may be combined to identify waveforms from explosions that are otherwise indistinguishable from background signal clutter and noise.

To study this problem, we collected electric, magnetic, acoustic and seismic records during parametric testing of solid explosives at Los Alamos National Laboratory (LANL). Our analyses focus on using correlation detectors to identify low amplitude waveforms generated by an above ground explosion in a noisy, cluttered signal environment. By fusing multiple detection statistics from all three phenomenologies through Fisher's combined probability test [27], we identify explosive sources otherwise undetectable even with optimal match

filtering operations. While previous work on near-surface explosions includes analyses of seismo-acoustic signals, almost no work to date has been done to include RF. This paper thereby demonstrates a semi-autonomous capability to identify explosions by including additional physical data underutilized by single signature correlation detectors.

1.2 Experimental Description

A series of 68 high explosive (HE) experiments (shots) were conducted at LANL using caseless charges of solid, bare Composition B in multiple configurations over a period of 3 weeks. Certain shot-parameters were controlled relative to reference tests during these experiments to study their influence on explosion signature variability [30]. These parameters included variable heights-of-burst, HE mass, HE shape, center versus surface ignition, substrate material, and explosive asymmetry. Several explosion phenomenologies were recorded during each shot, including acoustic/infrasound, optical, RF, and seismic emissions. Basic meteorological data was additionally collected from a nearby MET-station to monitor changes in the propagation media [28]. Because this paper focuses on the seismic, infrasound and RF data, we omit details regarding the collection of other signatures.

Electromagnetic data were recorded using 3 antennae collocated at a 113 meter slant distance from a fixed shot pit (Figure 1.1, top). These antennae measured the vertical component of the electric field (**E**) in high (20 MHz - 1 GHz) and low (2 MHz - 250 MHz) bands, while the magnetic field (**B**) was recorded at a 45° orientation from the **E** antennae in a low band (2 MHz - 70 MHz). Data logging was initiated by a capacitive discharge unit (CDU) triggering system and provided up to 400 msec data records, half of which measured pre-detonation background emissions. Coincident, high-frame rate video was recorded of each shot to visually document features of the fireball that could explain RF details (e.g. HE product ejecta, ground contact, fireball asymmetry).

Acoustic and seismic data were collected from collocated instruments a $\sim$ 1km horiztonal distance from ground zero at the Lower Slobbovia site (Figure 1.1, bottom). Acoustic data were recorded using a New Mexico Tech. infrasound sensor with a passband of 0.01-40 Hz, sampling at 1 kHz and logging to a RT130 digitizer and hard drive (described in [29]). Seismic data were recorded using a three-component Trillium Compact sensor with a $8 \cdot 10^{-3}$ Hz corner frequency, also sampling at 1 kHz and logging to the same RT130 digitizer and hard drive. Data time-stamps for both sensors were obtained from a local GPS antenna.

All experiments took place over/under dry sand, poultry netting (chicken wire) or a concrete pad. In this paper, we focus exclusively on two shots detonated above dry sand. The first shot consisted of a 4" cylindrical charge detonated at a 4m HOB on 05/13/2013, 21:50 UTC. The second shot consisted of a 8" cylindrical charge detonated at a 1m HOB on the following day (05/14/2013) at 18:25 UTC.

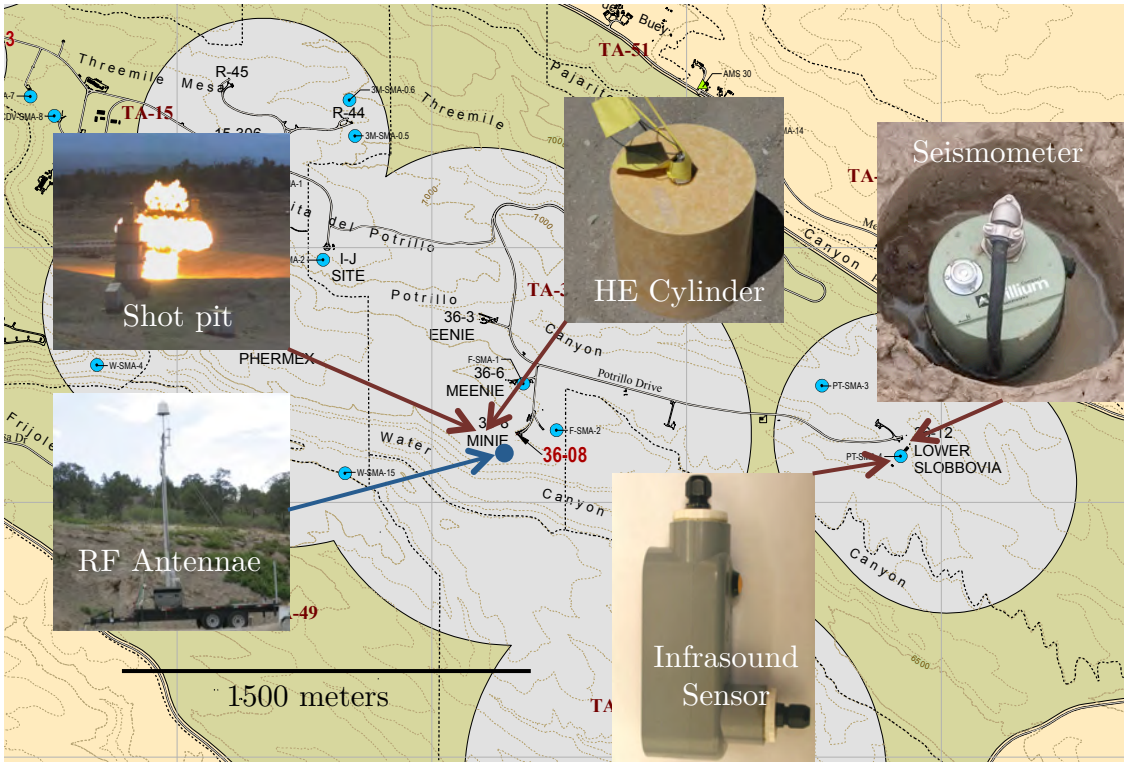

Figure 1.1: A map of the Los Alamos National Laboratory materials testing ranges, including the Minie site shot pit, proximal RF antennae, and the Lower Slobovia seismic and infrasound recording sites.

1.3 Geophysical Background

We summarize the geophysical processes of explosion-triggered waveform emission through the three phenomenologies below. Each respective signature description is self contained, and ordered by time of generation after HE detonation.

1.3.1 Electromagnetic Emissions

RF emissions from high explosives are related in timing and amplitude to physical properties of the explosive products, shock waves, and surroundings [21, 15, 10]. The explosion RF emission is usually characterized by self-similar, variable amplitude impulses with log-spaced peak-to-peak separation time (Figure 1.2). Analyses of time series and videos from 68 experiments performed at LANL (Section 1.2) reveal that the emissions from an uncased explosive are produced by distinct mechanisms in four broadly defined time intervals (10μsec - 100+ μsec). The first burst of RF emission (10-70 μsec; unrelated to the electric detonator) is associated with shock heating and ionization of the surrounding air. The second burst (70 μsec - 0.5 ms) coincides with the fireball resulting from combustion of explosive byproducts as they mix with air. A third interval of emission may occur when the shockwave reflects from the ground and re-heats the waning fireball (this may not always be observed, and will have timing dependent on height of burst). Direct shorting of ionized byproducts may also cause intense RF emission in the presence of a conductive ground plane [7]. Except for these conditions, the period from 0.5 ms to several 10s of milliseconds has little if any RF emission. A final period of emission starts around 25 ms and can last for 100s of milliseconds. This is evidently caused by pickup of environmental dust and subsequent collisional charging/discharging.

1.3.2 Acoustic and Infrasound Emissions

Explosions in air create large changes in local pressure over very short times, leading to the generation of shock waves that decay into sound (acoustic waves). The pressurized volume of gas within an explosively-driven air shock expands supersonically, resulting in a propagating pressure discontinuity (shock front) where the highly pressurized (and heated) air meets the ambient atmosphere [23]. As the pressure decays due to the increasing volume over which the energy is contained, the disturbance transitions to an acoustic wave of much smaller amplitude and leaves the surrounding medium unchanged. Characteristics of the shock wave and subsequent acoustic wave generated by the explosive-source depend on the explosive charge properties, in addition to the air through which the wave propagates. The low-frequency component of these signals ($\leq$ 20Hz) are conventionally described as infrasound [2].

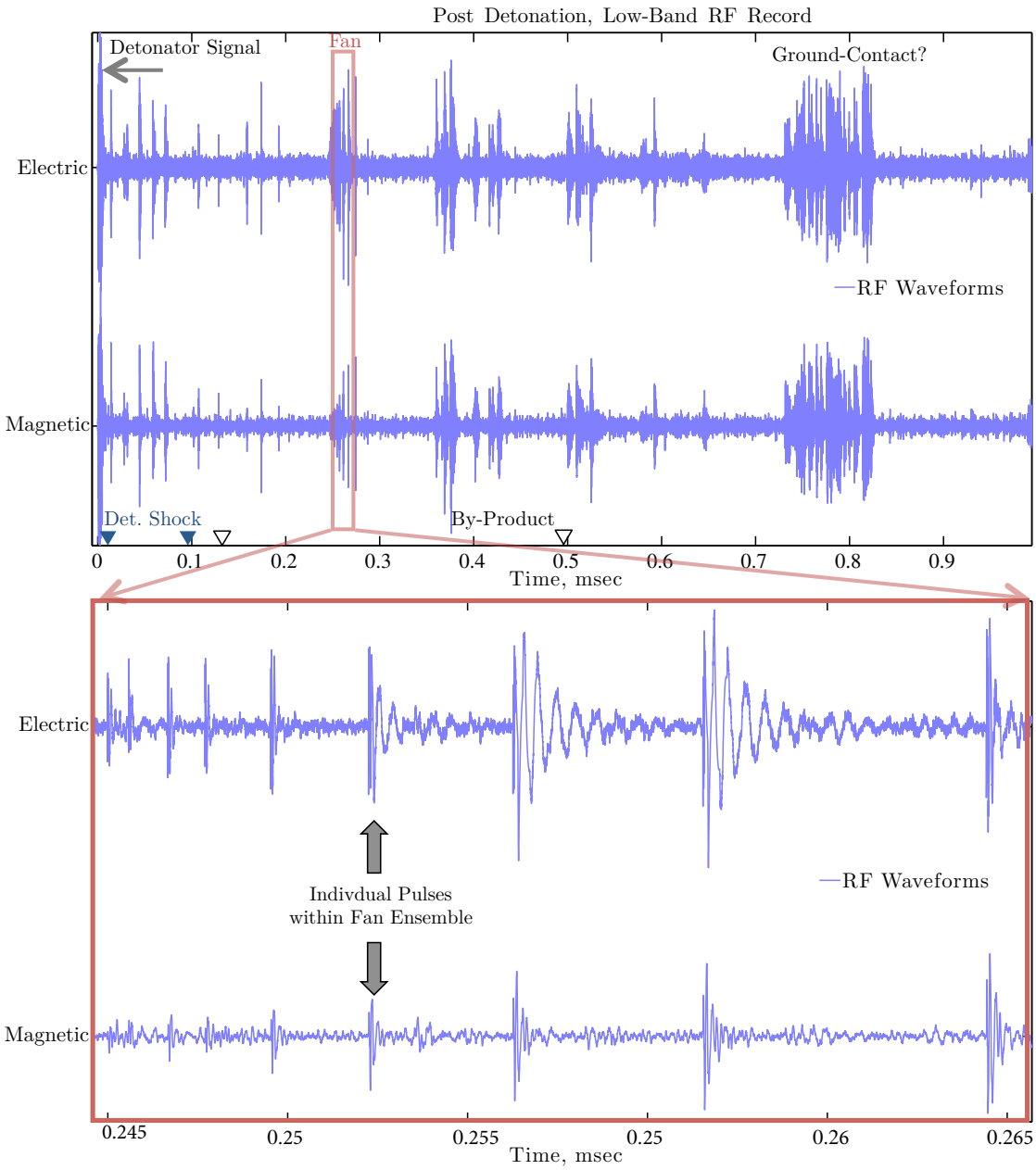

Figure 1.2: Electric and magnetic radio-frequency (RF) waveforms recorded during the detonation of an 8" cylindrical charge at a 1m HoB. All data are bandpass filtered between 2 and 156 MHz. **Top**: Emission features from zero to one msec after-detonation include emissions triggered by the detonation shock (blue markers), interaction of explosion by-products (black/white markers), and ostensibly fireball-ground contact; little signal is seen after 1msec (not shown). The red border indicates a fan. **Bottom**: A subset of repeated, pseudo-similar pulses from Top within the identified RF fan.

Explosively generated acoustic signals are recorded from two primary sources at different times after detonation. The initial acoustic arrival is driven by elastic ground displacement and produces a relatively weak signal that arrives coincidentally with ground-coupled seismic waves (Figure 1.3) [24]. The second source is the explosively-driven air shock, which develops into a broadband acoustic wave and produces much larger amplitudes compared with the first arrivals [2].

1.3.3 Seismic Emissions

Above-ground explosions of sufficient energy to induce ground cratering generate inelastic deformation that results in both direct and transverse displacement near ground zero [31]. This impulsive loading produces near discontinuous changes in stress that propagate outward as shock waves at super-elastic speeds [9]. The amplitude of these shocks decay and broaden through mechanical dissipation after a materially-dependent propagation distance (i.e., the elastic radius) and thereafter propagate as body waves (compressional and shear waves) and surface waves (e.g., ground roll). Seismometers record these ground-transmitted elastic waves as well as the following acoustic waves produced by air shocks. This includes ground impact from ballistic HE products traveling faster than the air shock, and coupled seismic-air waves arising from the feedback of ground-motion to acoustic energy [24]. The initial seismic arrivals generally produce smaller waveform amplitudes relative to the later arriving acoustic-signals, which appear coincident with the waveform recorded by the (collocated) infrasound receiver. The tails of these seismic waveforms are rich in scattered energy (coda) that extends over temporal durations that are long relative to the both the source time-function of the explosion and the associated infrasound waveforms. At least some of this scattered energy originates from ballistic material thrown out during cratering and impacting the ground. Unlike the direct arrivals, this energy is largely incoherent between the three recording channels of the seismometer (Figure 1.4).

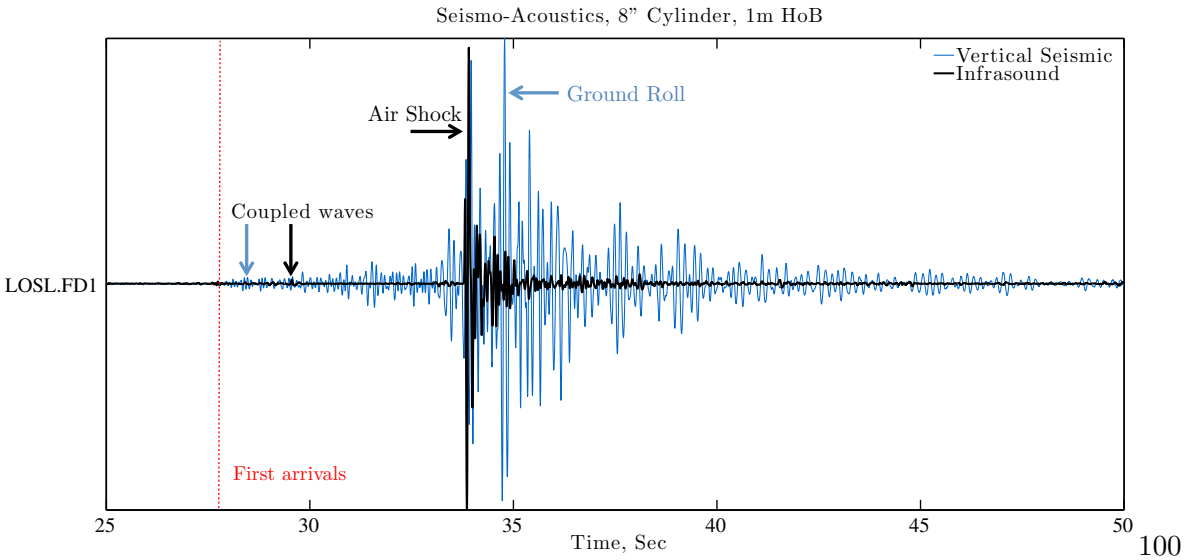

Figure 1.3: Vertical seismic velocity and infrasound waveforms recorded during the detonation of an 8" cylindrical charge at a 1m HoB, with arbitrary time origin. The small amplitude acoustic pulses appearing after the first arrivals and before the air wave are driven by seismic-acoustic feedback at the ground surface as described in Kitov et. al. [24]. The other labeled features are described in the text (Section 1.3.2).

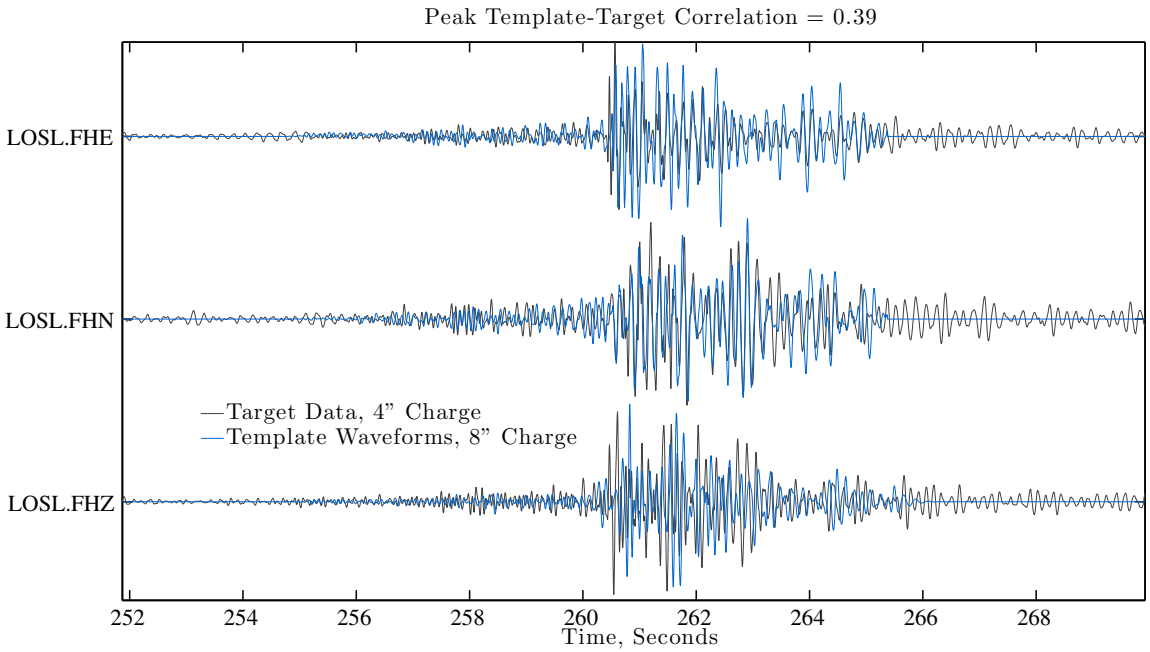

Figure 1.4: From top to bottom: east, north and vertical component seismic waveforms recorded during the detonation of an 8” cylindrical charge at a 1m HoB and aligned at maximum correlation (= 0.39) time delay with waveforms recorded during the detonation of a 4” cylindrical charge at a 4m HoB. The waveform produced by the 8” charge is zero-weighted where data amplitudes fall beyond a certain SNR value. Significant correlation between the waveform records of these two events requires waveform similarity and matching differential arrival times of phase segments. Vertical component waveforms exhibit the poorest cross-correlation, and are most sensitive to differences in charge HoB.

1.4 Methodology Overview

We summarize our data analyses in two self-contained sections. In Section 1.4.1, we derive a match-filtering detection statistic for identifying semi-similar, explosion triggered waveforms. We then demonstrate a process for combining the p-values from each associated statistic's estimated null distribution through Fisher's combined probability test (Section 1.4.2).

We first identified signatures of above ground explosions by applying multichannel correlation detectors to three measured phenomenologies in our data. Our approach was to select template waveforms recorded from reference explosions to compare against target data recording similar shots. To assemble these data sets, we primarily focused on two distinct experiments that included (1) a 4" cylindrical charge detonated at a 4m HoB and (2) an 8" cylindrical charge detonated at a 1m HoB, each conducted at the Minie shot pit (Figure 1.1). These data included 1000 sec of seismic and acoustic time series and 500 msec of continuous low-band RF data. Waveforms from the 8" charge were selected as reference/template data to compare against the 4" charge target data, which recorded the minimum amplitude explosion signals measured among the experiments. A preliminary comparison of these data demonstrated a significant waveform correlation between each respective signature (seismic data illustrated in Figure 1.5). To further reduce the amplitude of each target signature to < 0 dB of noise and challenge waveform detection, we added 10 randomly selected, commensurate records of scaled pre-shot noise to each time series recording the 4" charge (Figure 1.6) . We then digitally processed these noise-contaminated data using our correlation detectors to identify waveforms produced by the explosion (Section 1.4.1). Significant correlation between any two of our multi-channel data streams (e.g., seismic) required similarity in differential arrival times of pulse features within the event records (Figure 1.4). In contrast, seismic signals from two identical, hypothetical sources with different standoff distances would produce greater time delay between body and surface waves; sources at different azimuths would produce different energy partitioning between components of motion/propagation. Each of these effects degrade correlation between waveforms emitted from distinctly located sources. Therefore, our correlation detectors combined the detection, location and identification problems.

1.4.1 Correlation Detection: Theory and Computation

To automatically screen explosive signatures of HE tests from ambient noise and clutter, we developed phenomenology-specific multi-channel correlation detectors (matched filters). These detectors employ "template" waveforms recorded from reference events to scan multiple data streams for correlated signals indicative of similar emission sources [16, 12, 6, 34]. During each scanning operation, a detection statistic is computed from these data using

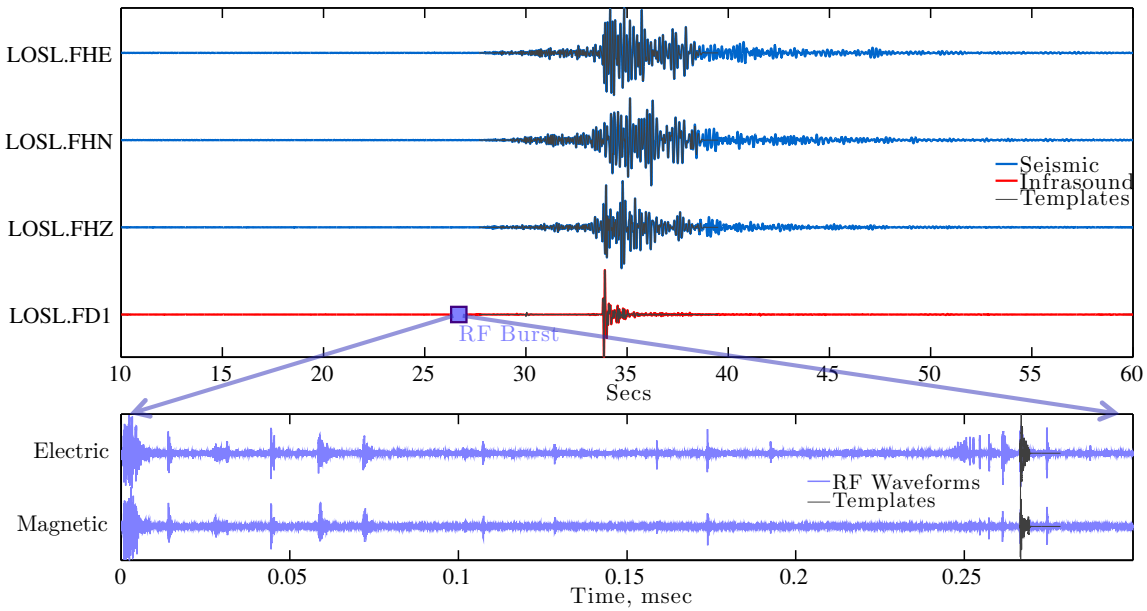

Figure 1.5: Waveforms recorded during the detonation of an 8" cylindrical charge at a 1m HoB. **Top**: East, north and vertical component seismic (blue) and acoustic/infrasound data (red), recorded over 50 seconds at station LOSL and bandpass filtered between 4 and 20 Hz. The initial waveform arrivals visible at $\sim$ 27 seconds record low amplitude, ground transmitted body and surface waves; the larger amplitude peaks at $\sim$ 34 seconds record the air wave. **Bottom**: High gain, low sample rate electric and magnetic data recorded over 0.3 msec following detonation and bandpass filtered between 2 and 156 MHz. Gray-colored data illustrate the template waveforms used in the associated correlation detector. The repeating pulses that appear after 0.25 msec comprise fan structures commonly observed during chemical explosions. Gray data indicate pulse segments within this fan that are used as templates in a correlation detector.

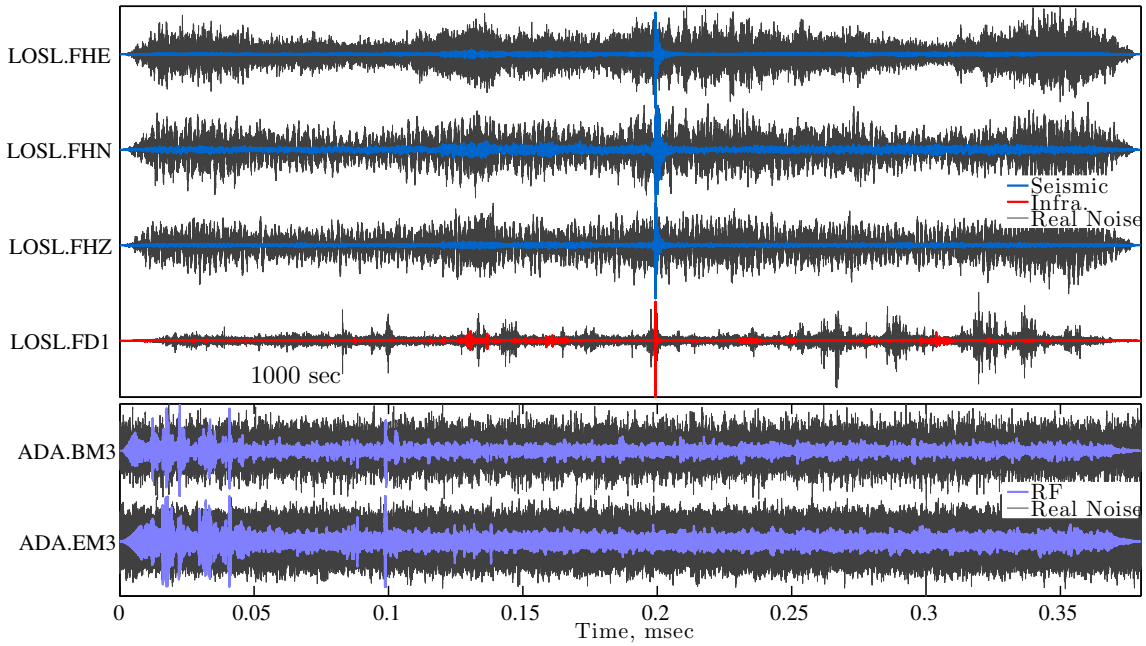

Figure 1.6: Waveforms recorded during the detonation of a 4" cylindrical charge at a 4m HoB, shown with observed noise. **Top**: East, north and vertical component seismic (blue) and infrasound data (red), recorded over 1000 seconds at station LOSL and bandpass filtered between 4 and 20 Hz. Gray data show 10 randomly selected commensurate windows of pre-shot data plotted on top of each other. These noise data were amplified $\sim 15\times$ and added to the original data to reduce the relative signal power to < 0 dB. **Bottom**: High gain, low sample rate electric and magnetic data recorded 0.38 msec following detonation. Superimposed gray data again show 10 randomly selected commensurate windows of pre-shot data. These noise data were scaled by $\sim \frac{1}{2}$ and added to the original data to reduce the relative RF signal power to that of the seismic and infrasound (<0 dB).

a statistical hypothesis test and compared to a threshold to evaluate the presence of a target waveform [20]. The significance of this threshold and the detector's performance depend on the data stream noise environment and the waveform signal complexity [37, 17]. Performance is also degraded by noise within this template, and any mismatch it has with the underlying target waveform [5, Appendix A]. However, if correlation templates have sufficiently high SNR and do match their targets, such detectors provide a demonstrably optimal detection capability [20, page 133].

Our data sets included L channel multi-sample rate shot records of wavefields $x(t) = [x_1(t), x_2(t), \cdots, x_L(t)]$ respectively sampled at intervals $\Delta t_1, \Delta t_2, \cdots, \Delta t_L$ and recorded over time T, at various gains. While our data set includes $1 \leq L \leq 3$, we present our method for any number of channels. We prepared these data for detection by pre-processing the seismic and acoustic data over $4 - 20$ Hz and the RF data over $2 - 156$ MHz, using 4-pole, minimum phase Butterworth filters (Figure 1.5); because our filter width restricted the acoustic data to infrasound-band frequencies, we use these terms interchangeably hereon. If a given signature's record included multi-sample rate data (e.g., RF), we synchronized the respective time series to a uniform sample rate Δt using an interpolation/upsampling scheme and arranged the resultant, commensurate vectors into column matrices. An L-channel signal is thereby expressed as $\boldsymbol{x} = [\boldsymbol{x}_1, \boldsymbol{x}_2, \cdots, \boldsymbol{x}_L] \in \mathbb{R}^{N \times L}$:

$$\boldsymbol{x} = \begin{bmatrix} x_1(0) & x_2(0) & \cdots & x_L(0) \\ x_1(\Delta t) & x_2(\Delta t) & \cdots & x_L(\Delta t) \\ \vdots & \vdots & \vdots & \vdots \\ x_1((N-1)\cdot\Delta t) & x_2((N-1)\cdot\Delta t) & \cdots & x_L((N-1)\cdot\Delta t) \end{bmatrix}, \tag{1.1}$$

where $T = N \cdot \Delta t$. The template waveforms containing the canonical explosion signatures were similarly pre-processed, upsampled, then Hamming tapered and arranged to form a data matrix $\boldsymbol{u} = [\boldsymbol{u}_1, \boldsymbol{u}_2, \cdots, \boldsymbol{u}_L] \in \mathbb{R}^{N \times L}$.

We consider two competing signal models for each data stream $\boldsymbol{x}$: waveform absent versus waveform present. Under the waveform-absent/null hypothesis $\mathcal{H}_0$, the post-processed data contain noise $\boldsymbol{n}_0$ that is parameterized by variance σ^2. Under the alternative/waveform present hypothesis $\mathcal{H}_1$, the data contain a sum of target signals $A\boldsymbol{u}$ and noise $\boldsymbol{n}_1$, where A is unknown and $\boldsymbol{n}_1$ is also parameterized by σ^2. In both cases, we assume that the data are drawn from Gaussian random processes, so that digitized samples of the noise distribute as $\boldsymbol{n}_k \sim \mathcal{N}\left(\boldsymbol{0}, \sigma^2 \boldsymbol{I}\right)$, where $\boldsymbol{n} \in \mathbb{R}^{N \times L}$ and $\boldsymbol{I} \in \mathbb{R}^{LN \times LN}$ $(k = 0, 1)$. We also assume that σ^2 does not significantly change within each detection window, so that this noise is statistically stationary over periods equal to the temporal width of the template (over $N \cdot \Delta t$ seconds). We state these competing hypotheses for a signal signature as:

$$\begin{aligned} \mathcal{H}_0: &\quad \boldsymbol{x} = \boldsymbol{n}_0 \sim \mathcal{N}\left(\boldsymbol{0},\, \sigma^2 \boldsymbol{I}\right) \quad \text{(noise present, } \sigma \text{ unknown)} \\ \mathcal{H}_1: &\quad \boldsymbol{x} = \boldsymbol{n}_1 + A\boldsymbol{u} \sim \mathcal{N}\left(A\boldsymbol{u},\, \sigma^2 \boldsymbol{I}\right) \quad \text{(noisy target present, } A, \sigma \text{ unknown)}, \end{aligned} \tag{1.2}$$

where each signature has a distinct pair of PDFs. In contrast to this model, our data were temporally correlated and non-uniform between channels. We accommodate for this correlation structure by parameterizing the probability density functions (PDFs) under each hypothesis with a scalar N_E that corrects for the effective number of statistically independent samples in $\boldsymbol{x}$; we discuss estimating N_E later. The PDFs under these respective hypothesis are then:

$$\begin{aligned} p_0\left(\boldsymbol{x};\, \mathcal{H}_0\right) &= \frac{1}{\left(2\pi\sigma^2\right)^{\frac{1}{2}\cdot N_E}} \exp\left[-\frac{||\boldsymbol{x}||_F^2}{2\pi\sigma^2}\right] \\ p_1\left(\boldsymbol{x};\, \mathcal{H}_1\right) &= \frac{1}{\left(2\pi\sigma^2\right)^{\frac{1}{2}\cdot N_E}} \exp\left[-\frac{||\boldsymbol{x} - A\boldsymbol{u}||_F^2}{2\pi\sigma^2}\right], \end{aligned} \tag{1.3}$$

where $||\boldsymbol{x}||_F = \sqrt{\mathrm{tr}\left(\boldsymbol{x}^{\mathrm{T}}\boldsymbol{x}\right)}$ denotes the Frobenius norm, which sums the two-norm of the data matrix columns.

We derive a detection statistic from the PDFs in Equation 1.3 using a generalized likelihood ratio (GLR) that includes maximum likelihood estimates for the data variances and unknown waveform amplitude. This ratio is tested against a threshold η to determine the absence/presence of a target waveform:

$$s\left(\boldsymbol{x}\right) = \frac{\max\limits_{A,\, \sigma_1}\{\, p_1\left(\boldsymbol{x};\, \mathcal{H}_1\right)\,\}}{\max\limits_{\sigma_0}\{\, p_0\left(\boldsymbol{x};\, \mathcal{H}_0\right)\,\}} \underset{\mathcal{H}_0}{\overset{\mathcal{H}_1}{\gtrless}} \eta, \tag{1.4}$$

where the maximum likelihood estimates are:

$$\begin{aligned} \hat{\sigma}_0 &= \frac{||\boldsymbol{x}||_F^2}{N_E} \\ \hat{A} &= \frac{\langle \boldsymbol{x}, \boldsymbol{u}\rangle_F}{||\boldsymbol{u}||_F^2} \\ \hat{\sigma}_1 &= \frac{||\boldsymbol{x} - \hat{A}\ \boldsymbol{u}||_F^2}{N_E}, \end{aligned} \tag{1.5}$$

and where $\langle \boldsymbol{x}, \boldsymbol{u}\rangle_F = \mathrm{tr}\left(\boldsymbol{x}^{\mathrm{T}}\boldsymbol{u}\right)$ denotes the Frobenius inner product. Substituting the quantities from Equation 1.5 into Equation 1.4 gives the decision rule:

$$s\left(\boldsymbol{x}\right) = \frac{\langle \boldsymbol{x}, \boldsymbol{u}\rangle_F}{||\boldsymbol{u}||_F||\boldsymbol{x}||_F} \underset{\mathcal{H}_0}{\overset{\mathcal{H}_1}{\gtrless}} \eta. \tag{1.6}$$

Mean channel correlation is often used as an alternative to $s\left(\boldsymbol{x}\right)$ in Equation 1.6 for multi-channel correlation. In this alternative formulation, correlation statistics are computed for each channel and then coherently averaged. However, this computation implicitly assumes

that the amplitude scaling (A) for a vector waveform can differ among the channels at a given sensor. This multiple scaling among distinct components of motion or propagation implies dissimilar template-target source mechanisms. We therefore prefer our more restrictive maximum likelihood approach, which assumes uniform scaling of the source mechanism among the components of motion.

Equation 1.6 represents the action of the detector in a given $N \times L$ sample detection window. To efficiently implement Equation 1.6 on many such windows, we scanned $\boldsymbol{u}$ against much longer, M-sample data streams $\boldsymbol{x} \in \mathbb{R}^{M \times L}$ as follows. First, we zero-padded $\boldsymbol{u}$ by concatenating its rows with a matrix of zeros $\mathbf{0} \in \mathbb{R}^{(M-N) \times L}$ to construct an "operational" template $\boldsymbol{u}_M = [\boldsymbol{u}\,;\,\mathbf{0}] \in \mathbb{R}^{M \times L}$ that dimensionally matched the data stream and was therefore suitable for computation. Next, we vectorized the template and data stream signals to avoid wasteful calculation of off-diagonal matrix products, in terms like $\langle \boldsymbol{x}, \boldsymbol{u}_M \rangle_F$. To do so, we multiplexed the data via the rule $\boldsymbol{x}\big[L(i-1)+j\big] = \boldsymbol{x}_{ij}$, so that each multichannel signal was reshaped by placing samples for the same time index along distinct channels into consecutive rows of a vector. We then computed $s\,(\boldsymbol{x})$ at single sample-shifts of the detection window by cross correlating $\dfrac{\boldsymbol{u}_M}{||\boldsymbol{u}||_F}$ against $\boldsymbol{x}$ in the frequency domain, and performing data stream normalization in the time domain. Finally, to obtain detections using $s\,(\boldsymbol{x})$, we established an acceptable false alarm probability of 10^{-8} with the Neyman Pearson criteria [20], for all three signatures, and defined a threshold for event declaration η:

$$10^{-8} = \mathrm{Pr}_{FA} = \int_{\eta}^{1} p_0\,(s\,;\,\mathcal{H}_0)\,ds \tag{1.7}$$

We computed the associated probability of detecting a target waveform by integrating $p_1\,(s\,;\,\mathcal{H}_1)$ over the acceptance region established by Pr_{FA}:

$$\mathrm{Pr}_D = \int_{\eta}^{1} p_1\,(s\,;\,\mathcal{H}_1)\,ds, \tag{1.8}$$

We reemphasize that each signature has a distinct pair of PDFs and associated detector performance.

To explicitly compute the detection threshold η, evaluate the probabilities in Equations 1.7 - 1.8, and compute p-values (Section 1.4.2), the distribution functions $p_k\,(s\,;\,\mathcal{H}_k)$ $(k = 0, 1)$ must be approximately known. We determine these PDFs from $s^2\,(\boldsymbol{x})$, which follows a central Beta distribution in the presence of only noise, and a noncentral Beta distribution in the presence of a combined waveform and noise [17]. We respectively denote the associated PDFs for $s^2\,(\boldsymbol{x})$ as $B\,(s;\,0,\,N_E)$ and $B\left(s;\,\frac{A^2}{\sigma^2},\,N_E\right)$ and perform a functional

transformation to obtain:

$$
\begin{aligned}
p_0\left(s\,;\,\mathcal{H}_0\right) &= |s| \cdot \left[B\left(s^2;\,0,\,N_E\right) + B\left(-s^2;\,0,\,N_E\right)\right] \\
p_1\left(s\,;\,\mathcal{H}_1\right) &= |s| \cdot \left[B\left(s^2;\,\frac{A^2}{\sigma^2},\,N_E\right) + B\left(-s^2;\,\frac{A^2}{\sigma^2},\,N_E\right)\right]
\end{aligned}
\tag{1.9}
$$

Each PDF in Equation 1.9 is parametrized by the waveform SNR and the effective number of independent data stream samples N_E that appears in Equation 1.3. Because $\boldsymbol{u}_M$ is zero-padded, this leaves only LN non-zero samples in an M-sample detection window. Often, $N_E \ll LN$, however. This occurs both naturally and through processing operations like bandpass filtering, which replace each sample with itself and a weighted sum of its neighbors and thereby introduce intra-sample statistical dependence. We therefore implemented an empirical estimator for N_E, denoted $\hat{N}_E$, to continuously update parameterizations for $p_0\left(s\,;\,\mathcal{H}_0\right)$ (see [37]). This estimator computes the sample correlation between the multi-channel template waveform $\boldsymbol{u}_M$ and several hundred psuedo-random, commensurate data vectors drawn from non-intersecting segments of post-processed, signal sparse data within $\boldsymbol{x}$. The sample variance $\hat{\sigma}_R^2$ of the resultant correlation time series is then computed using the 99.9% of the data by excluding 0.01% of the extreme left and right tails of its histogram. This provides the needed statistic to estimate N_E, given by:

$$
\hat{N}_E = 1 + \frac{1}{\hat{\sigma}_R^2},
\tag{1.10}
$$

and thereby compute the PDF $p_0\left(s\,;\,\mathcal{H}_0\right)$ and η.

In summary, each multi-channel correlation detector operates in a sliding window through the decision rule in Equation 1.6. The threshold for target declaration is computed by parameterizing the PDF $p_0\left(s\,;\,\mathcal{H}_0\right)$ (Equation 1.9) by $\hat{N}_E$ (Equation 1.10) for each respective signature and then inverting for η (Equation 1.7).

1.4.2 Computation of p-values

We fuse several independent correlation detection statistics into a single scalar time series by combining their respective p-values through Fisher's combined probability test. Given that a detector for phenomenology k produces an observed statistic $s_k(t_n)$ at time sample t_n, the respective p-value at that time sample is [35, 3]:

$$p_k(t_n) = \int_{s_k(t_n)}^{1} p_S(s_k; \mathcal{H}_0)\, ds_k, \tag{1.11}$$

where $p_S(s_k; \mathcal{H}_0)$ is the estimated null correlation distribution for random variable s_k and is parametrized by the data's effective degrees of freedom $\hat{N}_E$ (Equation 1.10). Temporally coincident p-values are each uniformly distributed and additive over M detectors and P signatures through a logarithmic transformation [3]. The samples of the resultant transformed time series then each follow a χ^2_2 distribution, while their coherent sum $Z_{M \cdot P}(t_n)$ gives the Fisher statistic:

$$Z_{M \cdot P}(t_n) \triangleq -2 \sum_{k=1}^{M \cdot P} \ln\left(p_k(t_n)\right) \sim \chi^2_{2M \cdot P}(t_n), \tag{1.12}$$

where the subscript on $Z_{M \cdot P}$ enumerates the added p-values, which are assumed to be statistically independent. Equation 1.12 is a statement of Fisher's combined probability test. It illustrates that moderate p-values from several temporally coincident and independent phenomenologies can be logarithmically superimposed to provide an anomalously large sum $Z_{M \cdot P}(t_n)$, at time t_n, in the presence of signal. The significance of this sum is determined by the cumulative right tail probability of its PDF and the associated inverse. We compute this inverse at a fixed right-tail probability of $\Pr_{FA} = 10^{-8}$ to also assign a threshold for event declaration α that is consistent with our correlation detectors:

$$F^{-1}_{\chi^2_{2M \cdot P}}\left(1 - 10^{-8}\right) = \alpha \tag{1.13}$$

where $F^{-1}_{\chi^2_{2M \cdot P}}(\bullet)$ denotes the inverse $\chi^2_{2M \cdot P}$ cumulative distribution function; our analysis includes $M = 1$, $P \leq 3$. While Equations 1.12 and 1.13 provides a practical framework for combining distinct detection statistics, aspects of our data collection challenge direct fusion of p-values. This is because both recording periods and sample rates differed substantially between the RF and other data. Whereas the seismic and infrasound data acquisition systems (DAS) continuously recorded at 1 msec sample rates, the associated low-band, RF DAS recorded only 400 msec at $2 \cdot 10^{-9}$ sec sample rates for each shot. To compare p-values among these three phenomenologies, it is necessary to bin RF correlation statistics to 1 msec sample rates and additionally extend the RF p-values to times outside the associated recording period. To perform binning, we implemented our RF correlation detector over

1 msec data windows to match seismic and infrasound sample intervals, and processed all available 500 msec data. We then computed the absolute maximum correlation value in each of the 500 resultant, 1 msec-long time series. The mean of these maxima thereby formed upper bounds on the expected ambient noise-correlation for times outside the RF recording period that were coincident with the seismic and infrasound data. Cumulatively, this procedure replaced RF correlation statistics with their maximal values in each 1 msec bin over the 500 msec record and replaced the remaining 1000 sec with the sample mean of the bin maxima. By applying these estimates, we intentionally overestimated the amplitude of the signal-absent detection statistic to provide a high background value for noise correlation. Our RF p-values therefore underestimate the relative difference between the signal absent versus signal present correlation statistic and should be considered conservative. We took this approach to (1) remove any assumptions about the presence/absence of template-similar RF signals and (2) avoid overestimating the detection capability of the corresponding Fisher statistic. In this specific case, Equation 1.12 must be modified to include the constant background correlation:

$$Z_3\left(t_n\right) = -2\ln\left(p_1\left(t_n\right)\right) - 2\ln\left(p_2\left(t_n\right)\right) - \bar{p}_R \sim \chi^2_4\left(t_n\right) + \bar{p}_R \tag{1.14}$$

where $\bar{p}_R$ denotes $-2\ln\left(\bar{p}\right)$ and $\bar{p}$ is the p-value computed from the sample mean of the bin maxima.

1.5 Results

Section 1.5.1 summarizes results from processing each noise-contaminated record of the 4" charge explosion with a phenomenology-specific correlation detector, using template waveforms recorded from the 8" charge explosion. Section 1.5.2 compares time series of Fisher statistics from seismic, combined infrasound and seismic, and finally, combined infrasound, seismic and RF data.

1.5.1 Correlation Detection Results

Figure 1.7 gives detection results computed from 1000 sec of noise-contaminated infrasound data recorded at LOSL (top). Our infrasound correlation detector misses the waveform triggered by the 4" cylindrical charge at a 10^{-8} false-alarm rate threshold and the respective detection statistic shows spurious peaks throughout the record that exceed the explosion-generated peak (middle). This means that lower thresholds required to correctly declare a template match would also trigger ~ 10 false alarms on signal clutter. We suspect these spurious correlation values are produced by experiment preparation activity at the shot pit. Despite such clutter, the estimated null for this correlation statistic (Equation 1.9, bottom) provides an excellent representation of the empirical null distribution (histogram), resulting in a relative fit error of $\sim 3\%$.

Figure 1.8 presents analogous detection results from seismic data recorded at LOSL over the same 1000 sec as the infrasound data, in identical format (top). While the correlation statistic peaks at the correct time, in contrast to the synchronous infrasound data, the threshold established by our prescribed 10^{-8} false alarm rate is too high relative to this peak to register a detection (middle). Our seismic data also include fewer spurious correlation values relative to the infrasound data, as expected from the relatively narrow empirical null distribution (bottom). We attribute this outlier-reduction to result from the larger time-bandwidth product afforded from multiple sensor channels, which increases the template's effective degrees of freedom (N_E, Equation 1.10). As with the infrasound data, the estimated null distribution (black curve) for the correlation statistic provides an excellent fit to the histogram ($\sim 3\%$ relative error).

Similar RF detection results are shown over 0.38 msec in Figure 1.9, with the remainder of the 500 msec omitted (top). In this case, our detector missed many of the target pulses produced by the explosion, but also correctly identified two that matched our template. Analysis of our RF data set revealed that each above-ground explosion generally fans composed of 10-50 such pulses that correlated well between different shots. One such fan-pulse was used as the template for our RF correlation detector. Consequently, single explosions may produce several RF correlation detection opportunities, in contrast to the

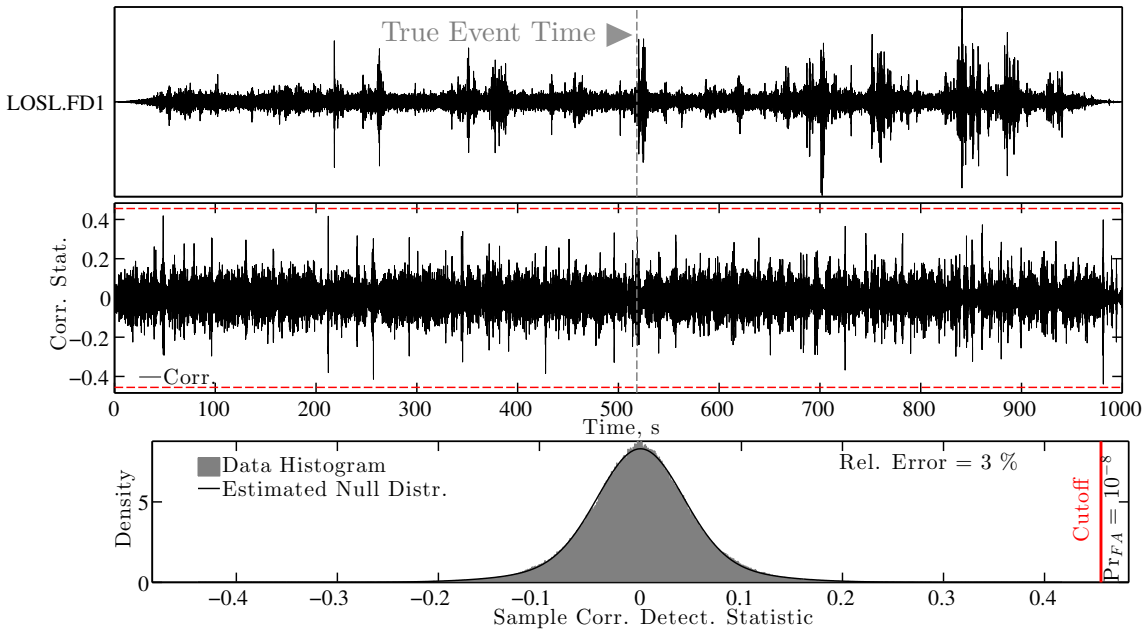

Figure 1.7: Acoustic correlation statistics computed from 1000 sec of data during the explosion of a 4" cylindrical charge at a 4m HoB, as measured by an infrasound sensor at station LOSL and contaminated by additive noise. **Top**: Noise-contaminated time series recorded during the explosion. The vertical gray line marks the true arrival time of the explosion waveform. Spurious signals beforehand and thereafter originate from human activity. **Middle**: Correlation statistic $s(\boldsymbol{x})$ computed from the detector template $\boldsymbol{u}_M$ and data at top. Horizontal red lines compare the threshold level η to data statistic amplitudes; positive η is consistent with a 10^{-8} false alarm probability. No detections were found. **Bottom**: The empirical null distribution (gray histogram) obtained by binning $s(\boldsymbol{x})$, compared to the predicted null distribution $p_0(s\,;\mathcal{H}_0)$ parameterized by $\hat{N}_E$ (black curve); the 3% relative error measures the distributional mismatch, and the red, vertical line marks the detection threshold η.

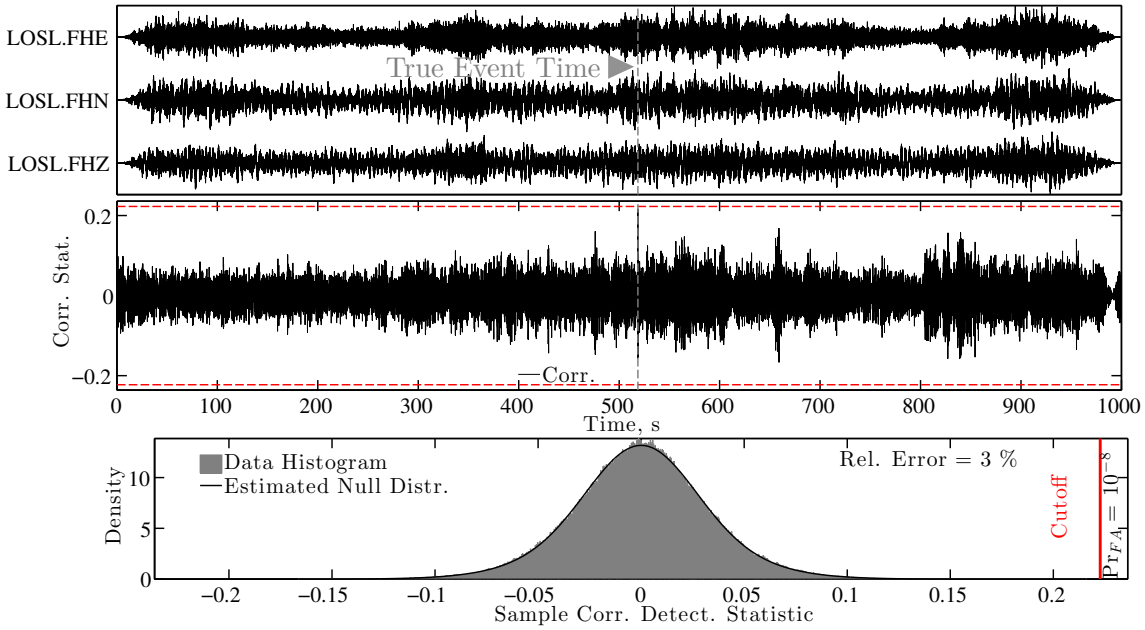

Figure 1.8: Seismic correlation statistics displayed in the same format as Figure 1.7, using data recorded at LOSL. Data are similarly contaminated along each respected channel with pre-shot background noise. As with the infrasound data, no detections were found.

single detection opportunities provided by the coincident seismic and infrasound records. To demonstrate the influence of these additional pulses, we simplistically assume that our target data contain K pulses with identical amplitudes and low probability of detection, $\theta = 0.16$. We then compute the probability of obtaining at least two detections, as observed in our data, from the binomial distribution:

$$\Pr\{\text{ at least 2 detections}\} = 1 - \binom{K}{0}\theta^0 \cdot (1-\theta)^K - \binom{K}{1}\theta^1 \cdot (1-\theta)^{K-1}. \qquad (1.15)$$

For $K = 10$, Equation 1.15 predicts approximately a 50% probability of detecting at least two pulses (compared to 16%). Therefore, the multiplicity of template-similar emissions effectively increases the probability of detecting a given explosion, despite the comparatively high threshold for event declaration obtained from our data. This threshold is illustrated by the empirical null distribution for the correlation statistic, which is extremely broad compared to that of the infrasound or seismic data (bottom). In this case, the high value arises from relatively a small N_E value that is induced by the short duration, transient RF template. Again, the fit error between the predicted and observed null distributions are exceptionally small ($\sim 3\%$)

1.5.2 p-Value Fusion Results

Figure 1.10 (bottom) shows the Fisher statistic $Z_1(t)$ computed from Equation 1.11 using the seismic correlation time series and corresponding null distribution (Figure 1.8, bottom). Like the correlation statistic, $Z_1(t)$ also peaks at the correct waveform arrival time for the explosion, but below the threshold imposed by the 10^{-8} right-tail probability constraint (Equation 1.13). By comparison, Figure 1.11 shows the result of fusing seismic and infrasound data together through the Fisher statistic, $Z_2(t)$. Whereas neither the seismic nor infrasound correlation detectors declared a template match, the fused statistic exceeds the respective threshold at the correct waveform arrival time and registers a detection. We assess the validity of this detection by comparing the empirical null PDF for $Z_2(t)$ (Figure 1.12, blue histogram) against the predicted χ^2_4 PDF (black curve) that was used to compute the detection threshold. This comparison provided excellent agreement, and increases our confidence in the significance of the detection. The high quality of the fit is likely attributable to the low relative error between the observed and predicted null distributions for the infrasound and seismic correlation statistics.

Figure 1.13 demonstrates the additional gain in detection capability from including the RF correlation data through the Fisher statistic $Z_3(t)$. Whereas the peak in $Z_2(t)$ registering the explosion exceeds its associated threshold by 1.4 units, the peak in $Z_3(t)$ exceeds its identically obtained threshold by ~ 15 units, or $10\times$ that of $Z_2(t)$. Figure 1.14 further shows an excellent agreement between the empirical null distribution (blue histogram) for

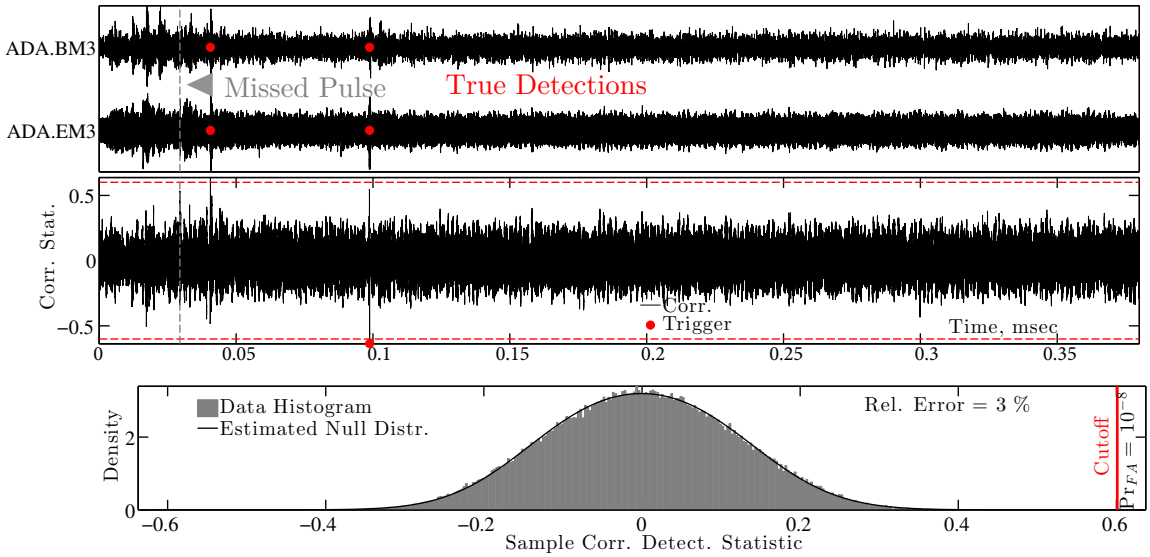

Figure 1.9: RF correlation statistics displayed in the same format as Figures 1.7 and 1.8, with electric and magnetic data from the RF antennae displayed over a 0.38 msec window. Data are also contaminated on each respective channel with pre-shot background noise. Two explosion-generated pulses are correctly detected, while many are missed; one miss is shown by the vertical gray line and triangular marker. Additional data, absent of target pulses, are not shown.

$Z_3(t)$ and the shifted χ^2_4 distribution predicted from theory (Equation 1.14, black curve). This relative increase in detection power likely underestimates the true increase due to the biased approach we adopted to compute the background, noise correlation (Section 1.4.2).

1.5.3 Statistical Influence of Wavefield Coupling

Our computation of $Z_2(t)$ neglected any dependency between seismic and infrasound data that was expected from physical coupling of the two wavefields at the ground surface (Figure 1.3) [2, 24]. Such coupling violates assumptions of independence on each signature's respective p-values, and artificially inflates the significance of the Fisher statistic [27]. We therefore assessed the potential correlation between the seismic and infrasound detection statistics by computing cross-correlograms between thousands of 1 second windows (e.g., correlations of correlation). We limited the correlation time-lags between the seismic and acoustic statistics from 0 to ± 4 seconds so that only potentially related portions of the signals were compared. This produced a sample set of high variance, near zero-mean correlation values (Figure 1.15). The absence of a significant non-zero mean suggests that the noise-contaminated seismic and infrasound correlation detection statistics were effectively independent. We had no analogous concern about seismic-RF or acoustic-RF wavefield dependency.

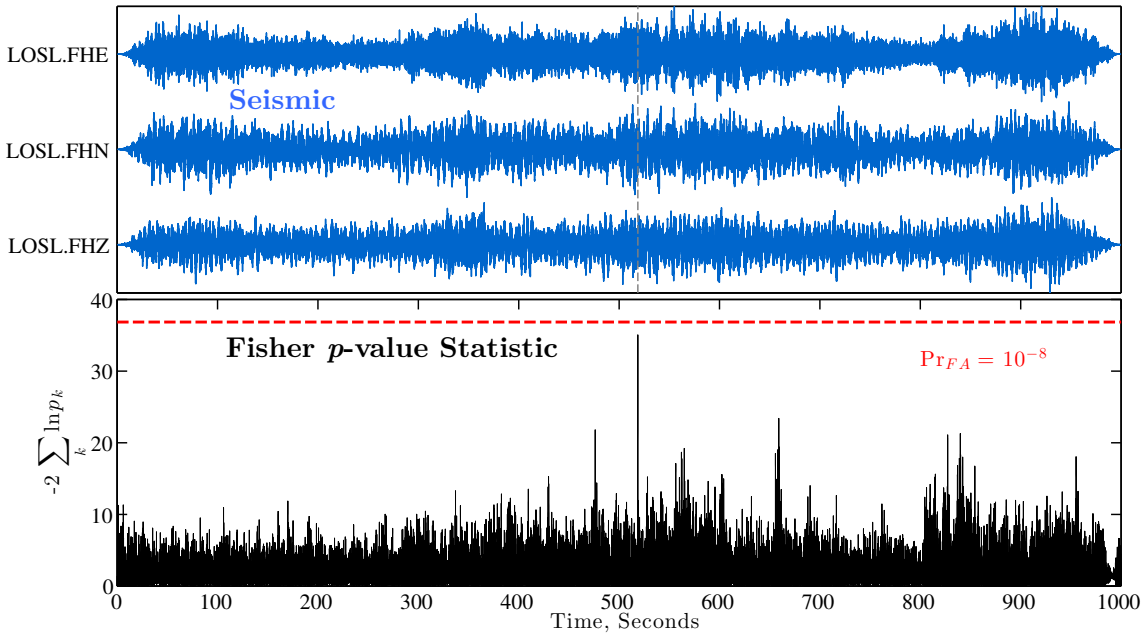

Figure 1.10: **Top**: The three channels of noise-contaminated seismic data recorded over 1000 sec at LOSL. The vertical gray line indicates the true seismic waveform arrival time. **Bottom**: The Fisher statistic time series $Z(t) = -2\ln(p(t))$ computed from the respective null $p_0(s\,;\mathcal{H}_0)$, parameterized by $\hat{N}_E$ (Figure 1.8, bottom). The horizontal red line indicates the inverse 10^{-8} right tail probability.

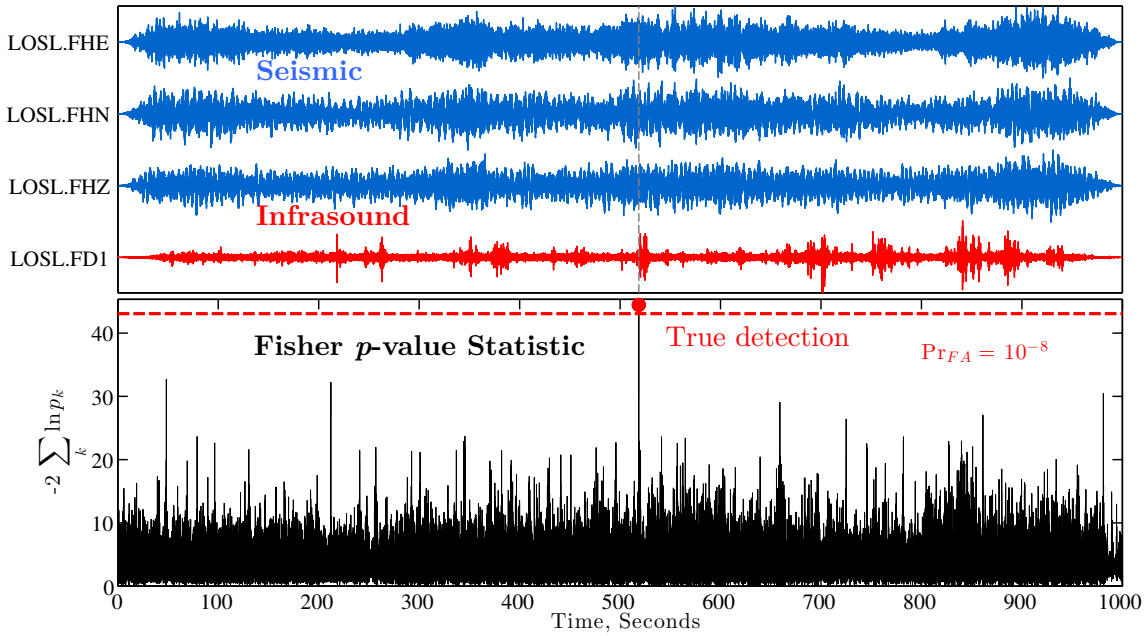

Figure 1.11: **Top**: Noise-contaminated seismic (blue) and infrasound data (red) recorded over 1000 sec at LOSL. The vertical gray line indicates the true waveform arrival times. **Bottom**: The Fisher statistic time series $Z(t)$ computed by adding $-2\ln(p(t))$ from the respective infrasound (Figure 1.7) and seismic data (Figure 1.8). The horizontal red line indicates the inverse 10^{-8} right tail probability. The filled, red circle marks a detection at the correct explosion time. Neither the infrasound nor seismic correlation detectors identified this explosion.

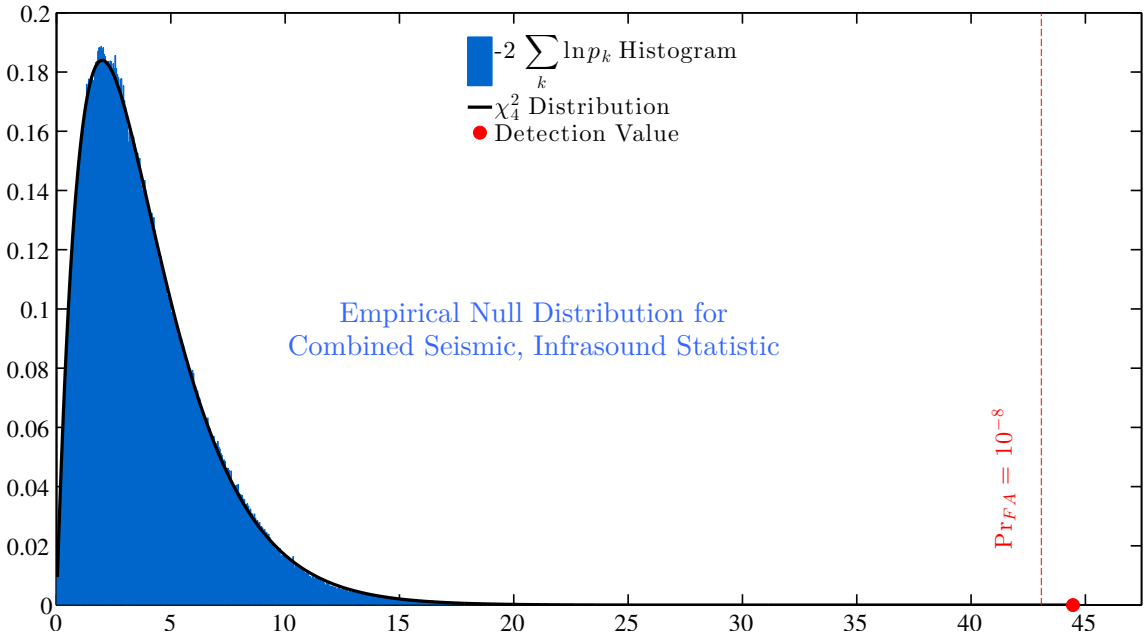

Figure 1.12: The empirical distribution for $Z(t)$ using seismic and infrasound data (histogram, blue) and the predicted distribution (black curve). The vertical red line indicates the inverse 10^{-8} right tail probability, and the red circle marks the peak detection value that corresponds with Figure 1.11.

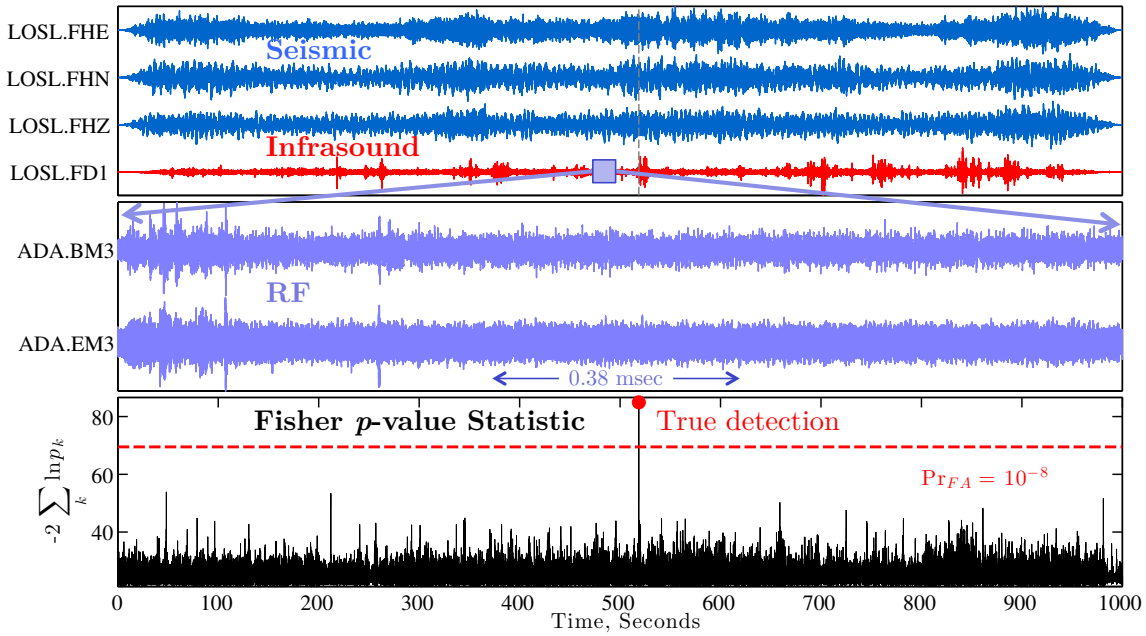

Figure 1.13: **Top**: Same as the top of Figure 1.11, with a square marker added to indicate explosion time and burst of RF emissions. **Middle**: The 0.38 msec of RF data from Figure 1.9 that includes known target pulses. **Bottom**: Similar to Figure 1.11, with $Z(t)$ computed from all three signatures. The peak detected at the correct event time exceeds that shown in Figure 1.11, relative to the background values.

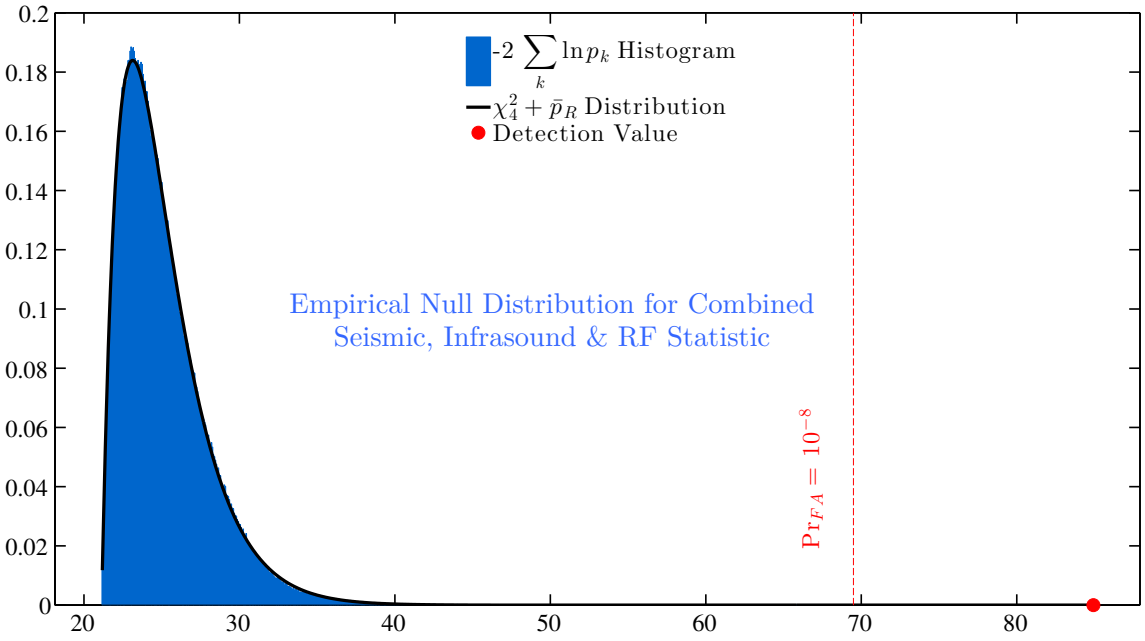

Figure 1.14: Similar to Figure 1.12, but data shown here include contributions from the RF p-values. The predicted distribution is additionally shifted by the mean, absolute maxima in correlation values that are computed over 500, 1 msec windows ($\bar{p}_R$, Equation 1.14). The detected peak in $Z(t)$ at the correct event time exceeds the threshold (vertical red line) by $\sim 15\times$ more than that shown in Figure 1.12

.

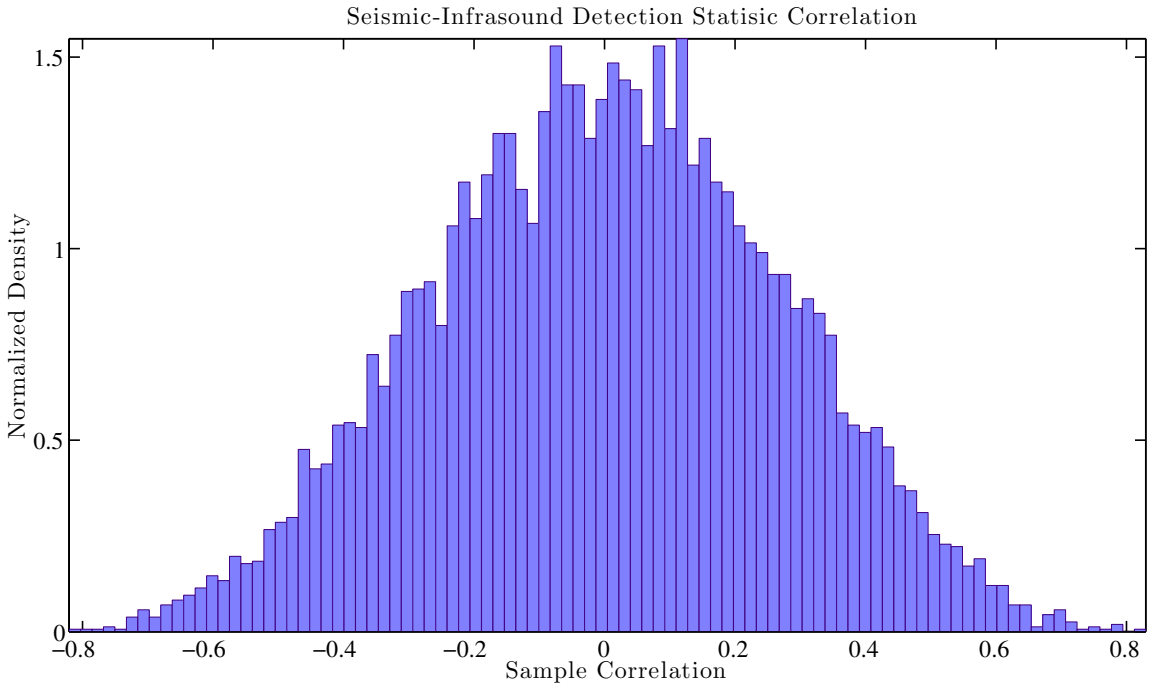

Figure 1.15: A histogram of cross correlation values computed between 1 second windows of infrasound and seismic correlation detection statistics, limited to 4 second relative time lags. The zero sample mean indicates a small or absent inter-signature correlation.

1.6 Discussion and Conclusions

We show that explosions undeclared by correlation detectors are identifiable when their respective detection statistics are fused through Fisher's combined probability test. Further, because these correlation detectors maximize the probability of registering known waveforms in Gaussian noise, our result also applies to STA/LTA, subspace, and other estimator-detectors [20]. Consequently, these alternative detectors would almost certainly fail to identify explosion-triggered waveforms in the same noise environment, and at higher false alarm rates. By combining their statistics with correlation values, however, they would likely contribute to further increase in overall detection capability and could be used to identify even smaller explosive sources [3]. In principle, such capability increase is predictable by comparing receiver operating characteristic (ROC) curves for each detector. However, more research is required to determine the Fisher statistic's distribution under the signal-present hypothesis to compute the associated ROC curves [19].

Fusing only two of the available correlation statistics still provided a gain in detection capability over single signatures. While our results were derived from local source standoff distances, the improvement obtained by combining seismic and acoustic data (Figure 1.11) is potentially significant to test-ban treaty verification missions. In these cases, networks of seismic and infrasound sensors, like those making up the International Monitoring System (IMS), are used to surveil evasively conducted nuclear tests in near-real time [11, 14]. Such networks often include collocated, three component seismic and infrasound sensors, similar to those deployed at LOSL. Fusing the statistics computed from such collocated receiver data can ostensibly increase a monitoring agency's capability to identify weak detonation signals, even absent single-signature detections.

Whereas there are several examples of prior seismo-acoustic analysis of surface explosions [1, 26, 25, 24], little open research exists on combining such data with electromagnetic signals [32, 18]. Our work suggests that the addition of RF and seismo-acoustic correlation statistics through data fusion can provide a significant improvement to explosion detection operations (Figure 1.13 versus Figure 1.11). This is partially due to the fidelity provided by RF emissions. Whereas explosively-triggered seismic waveforms at local distances consist of overlapping body, surface, and air waves (e.g., Figure 1.3), our explosion-triggered RF data exhibit fans comprised of $\sim$10-50 well-separated, similarly shaped transient pulses (Figure 1.2). We further found that pulses within such fans were often highly correlated against pulses within other fans that were triggered by different explosions. The multiplicity of these RF pulses implies that the probability of detecting at least one can be significant, even if the probability of detecting a single pulse is not. Including these features as templates in correlation detectors thereby increases the chance of explosion identification. In contrast, these pulses poorly correlated with ambient RF noise and registered no false

alarms, although our analysis was limited to 68, ∼400 msec shot records.

We suggest that co-deploying RF antennae at seismic/infrasound sites can lead to significant improvements in explosion monitoring capabilities, at least at local standoff distances. For such operations to be practical, the DAS will require internal triggering systems and precise time stamping to avoid continuous recording and thereby address onerous storage requirements at $\sim$ 1MHz $-$ 1GHz sample rates. Further, because our RF antennae was substantially closer to the source than the seismic/infrasound sensors, it is unclear if such pulses would be observable at greater ranges. Options for detecting substantially larger and optically-bright near-surface explosions may include integrating existent, space-borne observations from satellites [32]. Our ongoing work includes addressing such needs and investigating the physical mechanism of RF fan emission to determine its potential use for explosion discrimination and identification.

Our conclusions are conditioned on analyses that presume weak explosion signatures are representable by adding scaled (but real) noise to waveforms recorded from larger sources, thereby reducing each signature's noise-relative amplitude. For target and template waveforms produced by explosions with similar HoB, there are at least two justifications for this claim: (1) poor instrument emplacement or signal interference can dramatically reduce waveform detectability of small sources, and is equivalent to adding measurement noise as we have done [5], and (2) the impulsive source-time function of a much smaller explosive charge dominantly scales in amplitude. We consider this first point obvious, and concerning if deployment sites coincide with regions experiencing frequent thunderstorms or cultural noise. Regarding the second point, a diminished signal-to-noise ratio (SNR) is often equated to a reduction in a target event's seismic magnitude in semi-empirical analyses of seismic, multichannel correlation detectors [33, 34, 13]. More importantly, this practice has shown operational success in detection repeating earthquakes spanning ~ 3.5 seismic magnitude units [11], equivalent to waveform amplitude ranges of $\sim 3 \cdot 10^3$. In this case, no spectral rescaling was required. In our work, we reduced relative seismic amplitudes through the addition of 10 windows of pre-shot noise, which were then amplified by 15×. Assuming a maximum noise variance among these windows of σ_M, this addition reduces noise-relative waveform amplitudes by at most $\sigma_M \cdot 15\sqrt{10}$, or $< 47\times$ their original value. This reduction is therefore within established, moderate ranges of seismic source scaling. We emphasize that explosions with substantially different HoB will produce dissimilar waveforms because of differences in ground coupling and Rayleigh-wave-acoustic feedback [24]. With this caveat, similar arguments can be made for weak acoustic waveforms with low peak overpressure. While a lack of prior work precludes similar analysis of RF waveforms, we found that fan-pulse amplitudes in our data spanned two orders of magnitude among the different explosions, substantiating our scaling method.

Cumulatively, we demonstrate that multiple, fused explosion signatures can provide a su-

perior detection capability relative to that obtained by single-signature correlation detectors. Our results further show that Fisher's combined probability test provides an effective method for combining multiple geophysical observations. By summing such observable's statistics over additional independent detectors, as well as phenomenologies, even smaller sources become identifiable [3]. We therefore propose that implementing such multiple-signature fusion methods in routine monitoring operations can provide increased deterrence against clandestine weapon testing.

Bibliography

[1] Jürgen Altmann. Acoustic-seismic detection of ballistic-missile launches for cooperative early warning of nuclear attack. *Science and Global Security*, 13(3):129–168, 2005.

[2] Stephen J Arrowsmith, Jeffrey B Johnson, Douglas P Drob, and Michael AH Hedlin. The seismoacoustic wavefield: a new paradigm in studying geophysical phenomena. *Reviews of Geophysics*, 48(4), 2010.

[3] Stephen J Arrowsmith and Steven R Taylor. Multivariate acoustic detection of small explosions using fisher's combined probability test. *The Journal of the Acoustical Society of America*, 133(3):EL168–EL173, 2013.

[4] Philip S Blom. *Interaction of the Cyclonic Winds with the Infrasonic Signal Generated by a Large Maritime Storm*. PhD thesis, University of Mississippi, 2013.

[5] Joshua D Carmichael. *Melt-triggered seismic response in hydraulically-active polar ice: Observations and methods*. PhD thesis, University of Washington, 2014.

[6] Joshua D. Carmichael, Erin C. Pettit, Matt Hoffman, Andrew Fountain, and Bernard Hallet. Seismic multiplet response triggered by melt at blood falls, taylor glacier, antarctica. *Journal of Geophysical Research-Earth Surface*, 117:F03004, JUL 10 2012. PT: J; NR: 51; TC: 1; J9: J GEOPHYS RES-EARTH; PG: 16; GA: 974UL; UT: WOS:000306462800001.

[7] Melvin Alonzo Cook. *The science of high explosives*, volume 139. RE Krieger Pub. Co., 1958.

[8] Wo-Young Kim David P. Schaff and Paul G. Richards. Seismological constraints on proposed low-yield nuclear testing in particular regions and time periods in the past, with comments on "radionuclide evidence for low-yield nuclear testing in North Korea in april/may 2011" by Lars-Erik De Geer. *Science and Global Security: The Technical Basis for Arms Control, Disarmament, and Nonproliferation Initiatives*, 20(2-3):155–171, Oct 23 2012.

[9] Marvin D Denny and Dennis M Goodman. A case study of the seismic source function: Salmon and sterling reevaluated. *Journal of Geophysical Research: Solid Earth (1978–2012)*, 95(B12):19705–19723, 1990.

[10] Jonathan E Fine and Stephen J Vinci. Causes of electromagnetic radiation from detonation of conventional explosives: A literature survey. Technical report, DTIC Document, 1998.

[11] Steven J. Gibbons, Mathilde Bottger Sorensen, David B. Harris, and Frode Ringdal. The detection and location of low magnitude earthquakes in northern norway using multi-channel waveform correlation at regional distances. *Physics of the Earth and Planetary Interiors*, 160(3-4):285–309, MAR 16 2007. PT: J; TC: 14; UT: WOS:000244572200007.

[12] Steven J. Gibbons and Frode Ringdal. The detection of low magnitude seismic events using array-based waveform correlation. *Geophysical Journal International*, 165(1):149–166, APR 2006. PT: J; TC: 49; UT: WOS:000239689500013.

[13] Steven J. Gibbons and Frode Ringdal. Seismic monitoring of the north korea nuclear test site using a multichannel correlation detector. *IEEE Transactions on Geoscience and Remote Sensing*, 50(5):1897–1909, MAY 2012. PT: J; NR: 47; TC: 2; J9: IEEE T GEOSCI REMOTE; PN: Part 2; PG: 13; GA: 931GW; UT: WOS:000303205400015.

[14] Steven J. Gibbons, Frode Ringdal, and Tormod KvErna. Detection and characterization of seismic phases using continuous spectral estimation on incoherent and partially coherent arrays. *Geophysical Journal International*, 172(1):405–421, JAN 2008. PT: J; TC: 4; UT: WOS:000251669800030.

[15] Jeremiah Harlin and Robert Nemzek. Physical properties of conventional explosives deduced from radio frequency emissions. *Propellants, Explosives, Pyrotechnics*, 34(6):544–550, 2009.

[16] David B. Harris. A Waveform Correlation Method for Identifying Quarry Explosions. *Bulletin of the Seismological Society of America*, 81(6):2395–2418, December 1991.

[17] David B. Harris. Subspace Detectors: Theory. Technical Report UCRL-TR-222758, Lawrence Livermore National Laboratory, July 2006. ID: 316300514.

[18] Klaus-G Hinzen. Seismological analysis of a lightning strike. *Seismological Research Letters*, 83(3):492–497, 2012.

[19] H. M. James Hung, Robert T. O'Neill, Peter Bauer, and Karl Kohne. The behavior of the p-value when the alternative hypothesis is true. *Biometrics*, 53(1):pp. 11–22, 1997.

[20] Steven M. Kay. *Fundamentals of Statistical Signal Processing: Detection Theory*. Prentice-Hall Inc., Upper Saddle River, New Jersey, USA, 1st edition, 1998.

[21] Bob Kelly. Emp from explosions. *IS-4 Report Section, Group P-14 Los Alamos National Laboratory*, 1993.

[22] Vitaly I Khalturin, Tatyana G Rautian, and Paul G Richards. The seismic signal strength of chemical explosions. *Bulletin of the Seismological Society of America*, 88(6):1511–1524, 1998.

[23] Gilbert Ford Kinney and Kenneth Judson Graham. Explosive shocks in air. *Berlin and New York, Springer-Verlag, 1985, 282 p.*, 1, 1985.

[24] IO Kitov, JR Murphy, OP Kusnetsov, BW Barker, and NI Nedoshivin. An analysis of seismic and acoustic signals measured from a series of atmospheric and near-surface explosions. *Bulletin of the Seismological Society of America*, 87(6):1553–1562, 1997.

[25] Keith D Koper, Terry C Wallace, and Richard C Aster. Seismic recordings of the carlsbad, new mexico, pipeline explosion of 19 august 2000. *Bulletin of the Seismological Society of America*, 93(4):1427–1432, 2003.

[26] Keith D Koper, Terry C Wallace, Robert E Reinke, and John A Leverette. Empirical scaling laws for truck bomb explosions based on seismic and acoustic data. *Bulletin of the Seismological Society of America*, 92(2):527–542, 2002.

[27] James T Kost and Michael P McDermott. Combining dependent p-values. *Statistics & Probability Letters*, 60(2):183 – 190, 2002.

[28] Omar Marcillo, Stephen Arrowsmith, Rod Whitaker, Emily Morton, and W Scott Phillips. Extracting changes in air temperature using acoustic coda phase delays. *The Journal of the Acoustical Society of America*, 136(4):EL309–EL314, 2014.

[29] Omar Marcillo, Jeffrey B Johnson, and Darren Hart. Implementation, characterization, and evaluation of an inexpensive low-power low-noise infrasound sensor based on a micromachined differential pressure transducer and a mechanical filter. *Journal of Atmospheric and Oceanic Technology*, 29(9):1275–1284, 2012.

[30] Emily A Morton and Stephen J Arrowsmith. An empirical study of acoustic/infrasonic source and propagation effects using a large dataset of explosions. *The Journal of the Acoustical Society of America*, 134(5):4193–4193, 2013.

[31] John R Murphy. Near-field rayleigh waves from surface explosions. *Bulletin of the Seismological Society of America*, 71(1):223–248, 1981.

[32] AM Ortiz, SR Taylor, TJ Fitzgerald, and T Wallace. Rediscovering signal complexity discriminants: A preliminary study for application to regional seismic and radio fre-

quency signatures. Technical report, Los Alamos National Laboratory, Los Alamos, NM, United States, 2002. LA-UR-02-7657.

[33] David Schaff. Improvements to detection capability by cross-correlating for similar events: a case study of the 1999 xiuyan, china, sequence and synthetic sensitivity tests. *Geophysical Journal International*, 180(2):829–846, 2010.

[34] David P. Schaff. Broad-scale applicability of correlation detectors to China seismicity. *Geophysical Research Letters*, 36:L11301, JUN 3 2009. PT: J; UT: WOS:000266741600003.

[35] Steven R. Taylor, Stephen J. Arrowsmith, and Dale N. Anderson. Detection of short time transients from spectrograms using scan statistics. *Bulletin of the Seismological Society of America*, 100(5A):1940–1951, OCT 2010. PT: J; NR: 32; TC: 3; J9: B SEISMOL SOC AM; PG: 12; GA: 652KK; UT: WOS:000282005100007.

[36] Steven R Taylor, Stephen J Arrowsmith, and Dale N Anderson. Development of a matched filter detector for acoustic signals at local distances from small explosions. *The Journal of the Acoustical Society of America*, 134(1):EL84–EL90, 2013.

[37] Stephen Weichecki-Vergara, Henry L. Gray, and Wayne A Woodward. Statistical Development in Support of CTBT Monitoring. Technical Report DTRA-TR-00-22, Southern Methodist University, August 2001.